Stochastic entangled chain dynamics of dense polymer solutions

Demosthenes Kivotides,[a] S. Louise Wilkin, and Theo G. Theofanous
Department of Chemical Engineering, University of California, Santa Barbara, California 93117, USA

We propose an adjustable-parameter-free, entangled chain dynamics model of dense polymer solutions. The model includes the self-consistent dynamics of molecular chains and solvent by describing the former via coarse-grained polymer dynamics that incorporate hydrodynamic interaction effects, and the latter via the forced Stokes equation. Real chain elasticity is modeled via the inclusion of a Pincus regime in the polymer's force-extension curve. Excluded volume effects are taken into account via the combined action of coarse-grained intermolecular potentials and explicit geometric tracking of chain entanglements. We demonstrate that entanglements are responsible for a new (compared to phantom chain dynamics), slow relaxation mode whose characteristic time scale agrees very well with experiment. Similarly good agreement between theory and experiment is also obtained for the equilibrium chain size. We develop methods for the solution of the model in periodic flow domains and apply them to the computation of entangled polymer solutions in equilibrium. We show that the number of entanglements Π agrees well with the number of entanglements expected on the basis of tube theory, satisfactorily reproducing the latter's scaling of Π with the polymer volume fraction ϕ. Our model predicts diminishing chain size with concentration, thus vindicating Flory's suggestion of excluded volume effects screening in dense solutions. The predicted scaling of chain size with ϕ is consistent with the heuristic, Flory theory based value. © *2010 American Institute of Physics.* [doi:10.1063/1.3480682]

I. INTRODUCTION

The effects of topological chain motion constraints (entanglements) on the dynamics of polymeric fluids are important and challenging problem in statistical physics.[1–3] It is important because it governs the level of elastic stresses in viscoelastic flows[4] and challenging because an accurate account of entanglement effects on the statistical mechanics of polymer solutions has been proven to be a difficult task. On the one hand, many applications require just a macroscopic, continuum mechanical model.[5] On the other hand, there is microscopic, classical, Hamiltonian molecular dynamics that represents a fully adequate fundamental treatment.[6,7] Yet, it has not been easy to bridge the spatiotemporal scales between these two extremes while retaining the accuracy of the latter and the practical efficiency of the former.

Indeed, there are two intermediate coarse-graining regimes of the microscopic dynamics. Their mesoscopic character is due to the continuum medium phenomenology of the solvent in the corresponding space-time scales. In the finer Brownian limit regime,[8–21] polymers behave like stochastic, elastic, and uncrossable strings.[22] In principle, this level of description allows explicit detection and tracking of chain entanglements by appropriately adjusting the degree of coarse-graining of the fundamental equations. In the coarser yet still stochastic tube-theoretic regime, entanglements are modeled in a phenomenological way, i.e., via their effects on elastic stress levels. Tube theory models are an important part of the polymer physics.[22–26] Not only do they offer valuable insight into entangled solution dynamics but, by corre-

sponding to a coarse-graining level immediately below continuum dynamics, allow the derivation of constitutive laws via statistical physics methods.[27] Due to its heuristic nature, the tube theory requires significant empirical input pertaining to the stress relaxation plateau in step-strain experiments, as well as the values of phenomenological parameters gauging the strength of the various terms in the nonlinear stochastic differential equation that governs the coarse-grained chain conformation dynamics.[28,29] Further developments are needed in order to reliably tackle strong, nonequilibrium flows with dynamic strain rates.[30]

Our present work focuses instead on the finer mesoscopic dynamics regime. The physical models for this regime are significantly more complex than those of the Hamiltonian molecular dynamics. The latter involve only fundamental (in vacuum) interaction potentials (such as Lennard-Jones forces) that combine strong, short range repulsion with long-range (van der Waals) attraction between molecules.[31] The mesoscopic models necessarily involve coarse-grained (therefore solvent mediated) intermolecular interactions between polymer chains that are responsible for excluded volume effects, but in addition, also entropic elasticity and solvent hydrodynamic forces that are organized into drag and Brownian motion effects and are connected via the fluctuation-dissipation relation. The main issue is this: How can one ensure the uncrossability of polymer chains while employing coarse-grained excluded volume potentials? The crossing of two chains necessarily involves (due to outer electron shell overlap) hard, repulsion potentials which are not explicitly present in the formulas for the mesoscopic intermolecular forces. Although a detailed resolution of chain

---

a)Electronic mail: demos@engineering.ucsb.edu.

contact processes is not necessary, the qualitative (essentially topological) effects of chain uncrossability are important and are not tackled by the traditional phantom chain models of Rouse and Zimm.

There have been efforts to deal with the above pressing issues. In the context of stochastic dynamics, Larson and co-workers[32,33] correctly identified that bead-to-bead excluded volume forces are not adequate in securing chain uncrossability. Thus, they added strong, repulsive, short range potentials between springs. The advantage of their idea is that its computational implementation is relatively simple. On the other hand, there are some limitations. Hard potentials severely restrict the time steps allowed for numerical stability, thus the main advantage of the large evolution times that mesoscopic models allow in comparison with microscopic molecular dynamics is lost. Employing a soft, exponential, spring-to-spring potential allows larger numerical time steps, but does not guarantee chain uncrossability.[33] By default, the method does not provide direct geometric tracking of entanglement positions. A powerful although computationally much more demanding approach was initiated by Padding and Briels[34] in the context of polymer melts. They employed sophisticated, analytic geometry methods for the detection of spring crossings (entanglements) and the subsequent entanglement tracking. Kivotides *et al.*[35] extended the method of Padding and Briels while investigating the dynamics of chains in solution. They added several new elements that were deemed necessary in order to ensure the preservation of knots in chains placed in strong extensional flows. Employing their model, Kivotides *et al.* showed that knots slow down the rate of polymer stretching, thus cause a slower build-up of elastic stresses in the fluid and, consequently, smaller elastic effects on the flow.

The entangled chain dynamics (ECD) model of Kivotides *et al.* has a number of limitations: (a) it assumes unbounded flow domains, (b) it tackles good solvent solutions yet employs the finitely extensible nonlinear elastic (FENE) law that refers to ideal chains,[2] and (c) it requires adjustable constants in order to predict longest relaxation time and equilibrium chain sizes in agreement with experiment. Moreover, (d) the quantification of the relative merits of geometric entanglements and physical intermolecular forces on the overall excluded volume effects has not been systematically studied. Point (a) limits the applicability of the model to dilute solutions since one cannot define polymer mass concentrations in unbounded domains. Admittedly, the most important entanglement effects appear in dense solutions, thus, in this work, we extend the model to periodic flow domains. In doing this, we have developed the necessary analytic geometry and informatics methods for the detection and tracking of entanglements in a periodic cube. This extension significantly increases the computational complexity of an already algorithmically demanding method, but allows one to unambiguously study polymer mass concentration effects with ECD. Responding to point (b), we employ here a constitutive law of entropic elasticity that incorporates real chain effects according to the Pincus scaling.[36] We then show that the new ECD reproduces the experimental equilibrium longest relaxation time and chain size without the need of adjustable con-

stants, i.e., by simply requiring as input standard polymer and solvent material properties, thus addressing point (c). Moreover, to elucidate point (d), we systematically analyze the relative merits of entanglements and (coarse-grained) intermolecular forces on the overall excluded volume effects showing that both contributions are necessary in order to achieve agreement between theory and experiment while avoiding parameter tuning. Finally, we demonstrate our methods by analyzing finite concentration effects on the number of entanglements and polymer chain size in equilibrium dense solutions.

II. MODEL OF ENTANGLED POLYMER SOLUTION DYNAMICS

Our analysis is based on a self-consistent model of dense polymer solution physics. The model incorporates the Brownian limit of the underlying Hamiltonian dynamics thus, the solvent is described by continuum mechanics and the polymers by coarse-grained molecular dynamics. In the low Reynolds number flows we are considering here, the essential physics can be summarized as follows: polymer motion stirs the solvent and, in turn, solvent motion drags the chains with it. Accordingly, the solvent obeys a forced Stokes equation

$$\boldsymbol{\nabla} p(\mathbf{x}) - \eta_s \nabla^2 \mathbf{u}(\mathbf{x}) = \boldsymbol{\rho}(\mathbf{x}), \tag{1}$$

$$\boldsymbol{\nabla} \cdot \mathbf{u}(\mathbf{x}) = 0, \tag{2}$$

where $\mathbf{x}$ denotes a space position, p is the pressure, $\mathbf{u}$ is the solvent velocity, and η_s is the solvent dynamic viscosity. The delta function forcing per unit volume is $\boldsymbol{\rho}(\mathbf{x}) = \sum_{\kappa=1}^{N} \mathbf{f}_\kappa \delta(\mathbf{x} - \mathbf{x}_\kappa)$, where $\mathbf{f}_\kappa$ is the force exerted by the polymer segment (bead) located at $\mathbf{x}_\kappa$ on the fluid and N is the number of segments whose sum comprises the total polymer length within the flow domain. In all computations presented in this work, $\boldsymbol{\rho}(\mathbf{x})$ is the sole source of solvent motion.

There are N_c polymer chains in the flow domain. For full details on the mathematical terminology pertaining to the description of their conformation, Ref. 35 could be consulted. Every polymer chain is discretized into N_b massive beads (linked Lagrangian markers) that are connected by $N_s = N_b - 1$ massless springs ($N = N_c N_b$). The governing Langevin equation is

$$m_b \frac{\mathrm{d}v_i}{\mathrm{d}t} - {}^e\mathrm{F}_i - {}^m\mathrm{F}_i = {}^h\mathrm{F}_i + {}^t\mathrm{F}_i, \tag{3}$$

where m_b denotes the bead mass and $v_i = \mathrm{d}r_i/\mathrm{d}t$ denotes the velocity corresponding to bead coordinate r_i. The left hand side includes (in turn) polymer inertia, elastic and (coarse-grained) intermolecular forces. The right hand side represents the nonlinear coupling between chains and solvent, i.e., the hydrodynamic drag and thermal fluctuation forces. The strengths of these two effects, which are the polymer equivalent of the source $\boldsymbol{\rho}(\mathbf{x})$ in the dynamics of the solvent, are connected via the fluctuation-dissipation relation. The intermolecular force (IMF) ${}^m\mathrm{F}_i$ is one of the contributors to excluded volume effects. The other contributor comes from entanglements between chains and the resulting ECD.[35]
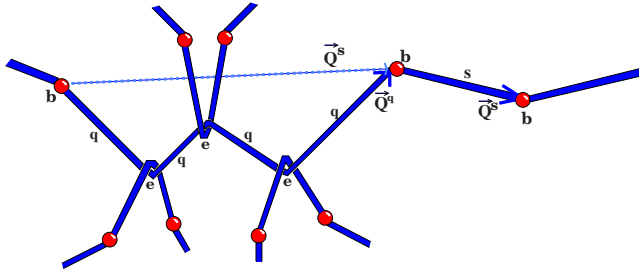
FIG. 1. A typical entangled chain configuration. The symbols are as follows: **b** indicates a bead, **e** is an entanglement, **q** is a spring or a portion of a spring, i.e., a connector between any beads or entanglements (with corresponding vector $\mathbf{Q}^q$), and s is a spring (with corresponding vector $\mathbf{Q}^s$). Beads and entanglements are collectively called objects.

Next, we shall discuss in detail the forces governing polymer motion. We are concerned with linear chains, and the relevant terminology is explained in Fig. 1. The modeling of the forces does not employ any adjustable constants. Its input includes only material quantities: the temperature of the solution T, the dynamic viscosity of the solvent η_s, the polymer molar molecular mass M, the Kuhn length b_K, the Kuhn monomer molar molecular mass M_K, and the Kuhn monomer excluded volume v_{ev}. All these quantities can be deduced from experiments as explained in Ref. 21. In this context, we note that the number of beads per chain N_b is not another adjustable parameter in our model. Instead, the value of N_b fixes the degree of coarse-graining in the system. That is, for each problem, one simply decides what level of coarse-graining is appropriate for resolving the frequencies and wavenumbers of interest to them. The various formulas of the theory automatically adjust to the chosen coarse-graining level, and the model is fully determined without any further special input. Later on, we demonstrate the robustness of longest relaxation time and chain size predictions upon N_b variations.

A. Coarse-grained intermolecular forces

We denote by $^m\mathrm{F}_i$ the component (corresponding to r_i) of the bead-to-bead excluded volume force $^m\mathbf{F}^b$ (Ref. 35),

$$^m\mathbf{F}^b = -\partial^m\phi^b/\partial\mathbf{r}^b, \tag{4}$$
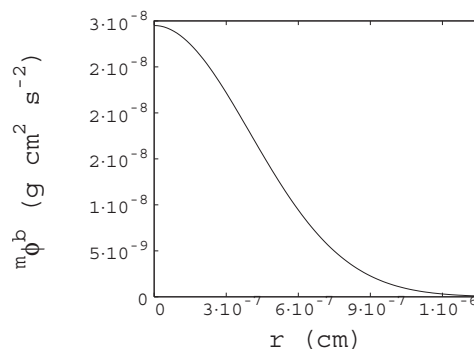
$$^m\phi^b = \sum_{b1=1, b1 \neq b}^{N_c N_b} \alpha e^{-(\mathbf{r}^{b1}-\mathbf{r}^b)\cdot(\mathbf{r}^{b1}-\mathbf{r}^b)/\delta^2}, \tag{5}$$

where $\mathbf{r}^b$ denotes the position of bead b, $\alpha = k_B T N_{K,s}^2 v_{ev}/R_s^3$ is the potential strength, and $\delta = R_s/2$ is the potential range. In these relations, k_B is the Boltzmann constant, $N_{K,s} = M/(M_K N_s)$ is the number of Kuhn lengths per spring, and R_s is the equilibrium spring size which is computed via Flory mean-field theory and its renormalization group refinements: $R_s = b_K(v_{ev}/b_K^3)^{2\nu-1}N_{K,s}^\nu$, where $\nu = 0.588$ ($\nu = 0.5$ in a theta solvent). The variation of the excluded volume potential with distance is depicted in Fig. 2 (left).

B. Viscous drag and thermal fluctuation forces

By neglecting the effects of short range lubrication interactions in the computation of resistance tensors,[20] the hydrodynamic force becomes[20,37,38]

$$^h\mathrm{F}_i = -\sum_{j=1}^{3N_c N_b} \zeta_{ij} v_j, \tag{6}$$

where ζ_{ij} is the hydrodynamic friction tensor. Denoting by $\boldsymbol{\mu} = \boldsymbol{\zeta}^{-1}$ the mobility tensor, $v_j = -\sum_{j=1}^{3N_c N_b} \mu_{ji} \, ^h\mathrm{F}_i$ is the Stokes flow induced by $N_c N_b$ point forces $^h\mathbf{F}^b$ at the bead positions. The thermal fluctuation force $^t\mathrm{F}_i$ is[20]

$$^t\mathrm{F}_i = \sum_{j=1}^{3N_c N_b} a_{ij} f_j, \tag{7}$$

where a_{ij} are related to ζ_{ij} by the relation

$$\zeta_{ij} = \frac{1}{k_B T} \sum_{l=1}^{3N_c N_b} a_{il} a_{jl}, \tag{8}$$

and f_j are described by a Gaussian distribution with mean and covariance

$$\langle f_i \rangle = 0, \quad \langle f_i(t)f_j(t')\rangle = 2\delta_{ij}\delta(t-t'), \tag{9}$$

where $\delta(t-t')$ is the delta function. The hydrodynamic interactions are parametrized by the bead radius a which, since the bead mass represents the mass of the chain segment corresponding to a spring, we choose $a = R_s/2$.
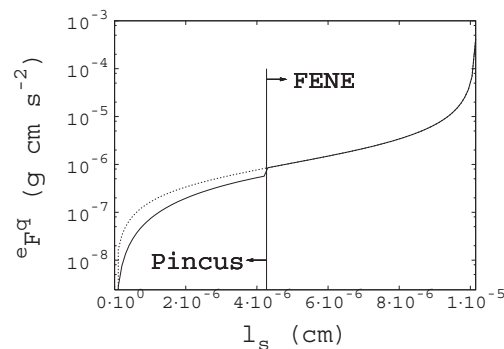

FIG. 2. Left: variation of the coarse-grained intermolecular force potential $^m\phi^b$ with distance r. Right: the force-extension-curve corresponding to the employed elasticity constitutive law. The latter combines a small extension Pincus regime with a large extension FENE regime. For comparison, we have also included the small extension part of the FENE law curve (dotted line).
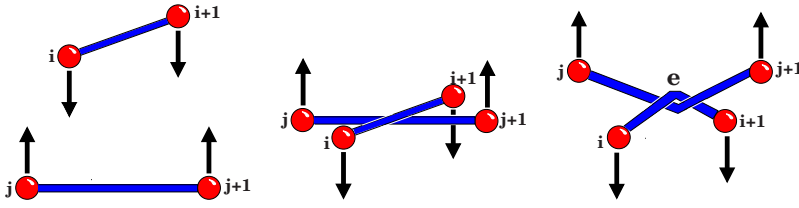
FIG. 3. A connector with end-points i, $i+1$ entangles with connector j, $j+1$.

C. Elastic forces

The elastic force ^eF_i is equal to the difference of the elastic forces $^e\mathbf{F}^q$ of the connectors that are attached to the bead corresponding to r_i. We describe the connector elastic force by a constitutive law that is appropriate for real chains. In particular, denoting the spring length by ℓ_s, the maximum spring length by $\ell_0 = N_{K,s}b_K$ ($L_0 = N_s\ell_0$ is the maximum chain length) and their ratio by $r = \ell_s/\ell_0$, we identify two regimes in the force-extension curve (FEC) of a real chain:[2,36,39] the small extension $r < r^\star$ regime where the Pincus FEC law is valid and the $r \geq r^\star$ regime where the probability density function of the chain end-to-end distance of an ideal chain are (approximately) equal to the one for a real chain, thus the standard FENE law is appropriate. As discussed in Ref. 2, $r^\star \approx 0.42$. Consequently, we have

$$^e\mathbf{F}^q = \begin{cases} \dfrac{3k_BT}{2b_K(1-\nu)}\left(\dfrac{\ell_s}{\ell_0}\right)^{\nu/(1-\nu)}\hat{\mathbf{Q}}^q, & r < r^\star \\[4mm] \dfrac{3k_BT}{N_{K,s}b_K^2}\left(\dfrac{\ell_s}{1-(\ell_s/\ell_0)^2}\right)\hat{\mathbf{Q}}^q, & r \geq r^\star, \end{cases} \quad (10)$$

where $\hat{\mathbf{Q}}^q$ is the unit vector along connector q. Focusing on the $r < r^\star$ regime, we note that when $\nu = 0.5$, one obtains the linear Hooke elasticity of an ideal chain. On the other hand, employing Flory's mean-field theory value $\nu = 3/5$, one recovers the Pincus elasticity law $\ell_s \sim f^{2/3}$. As we shall show, this has a significant impact on the resulting physics. In the computations, we employ the renormalization group value $\nu = 0.588$. The force-extension-curve corresponding to our composite constitutive law is depicted in Fig. 2 (right).

D. Entanglements

Entangled chain dynamics is discussed in great detail in Refs. 34 and 35. Here, we give a working summary in order to later explain better our method for the solution of ECD in periodic flow domains. First, we note that in contrast to beads, the number of entanglements in the system is a dynamic quantity. So we need two computational operators: (a) an operator that adds or removes entanglements and (b) an operator that acts on existing entanglements and moves them to a new position. The former encodes necessarily a jump process while the latter is a continuous one. The creation/annihilation operator is based on the following geometric picture. Any two consecutive objects (beads or entanglements), i and $i+1$, define a connector (Fig. 3). The motion of the end-points i and $i+1$ defines the connector's trajectory between consecutive time instances. For every pair of connectors (with j and $j+1$ the end-points of the second connector), the creation operator tracks the entanglement volume[34]

$$V^{ij} = (\mathbf{r}^i - \mathbf{r}^j) \cdot ((\mathbf{r}^{i+1} - \mathbf{r}^i) \times (\mathbf{r}^{j+1} - \mathbf{r}^j)), \quad (11)$$

and when V^{ij} (Fig. 3) changes sign, it adds an entanglement between the two connectors. Reversing in time the process of Fig. 3 explains the workings of the entanglement annihilation operator. Some subtle details involved in this simple idea are discussed in Ref. 35. In order to compute entanglement motion we assume, following Padding and Briels,[34] that its characteristic time scales are much faster than the time scales of bead motion, so the new entanglement positions are found by minimizing the elastic potential energy of the polymer system while keeping the bead positions constant. We minimize the sum of the spring potential energies, taking care of the different FEC scaling regimes

$$^e\Phi = \sum_{s=1}^{N_cN_s}{}^e\phi^s, \quad {}^e\phi^s = \begin{cases} \alpha\ell_s^{\mu+1}/(\mu+1), & r < r^\star \\[2mm] -\dfrac{H\ell_0^2}{2}ln|1-(\ell_s/\ell_0)^2|, & r \geq r^\star, \end{cases}$$

$$(12)$$

where $\alpha = (3k_BT/[2b_K(1-\nu)])(1/\ell_0)^{\nu/(1-\nu)}$, $\mu = \nu/(1-\nu)$, and $H = 3k_BT/(N_{K,s}b_K^2)$ is the elastic constant for an ideal chain.

III. INFINITELY DILUTE SOLUTIONS

Although the treatment of hydrodynamic forces is standard in our model, there are new aspects related to coarse-grained intermolecular forces, entangled chain dynamics, and the elastic constitutive law (Pincus-FENE). Notably, it is the combined action of the first two above factors that is responsible for excluded volume effects. Moreover, by requiring only standard material properties as input, our model does not include any adjustable constants, thus, it is instructive to investigate how well it compares with experiment.[21] Our tests refer to an aqueous polyethylene oxide (PEO) solution at $T = 293.15$ K. The corresponding solvent viscosity is $\eta_s = 0.01$ g cm^{-1} s^{-1}. The input properties of the PEO molecule are $M = 1 \times 10^6$ Da, $b_K = 7.37 \times 10^{-8}$ cm, $M_K = 90.49$ Da, and $v_{ev} = 150.31 \times 10^{-24}$ cm^3.[2,21] A single, stretched polymer chain is allowed to relax. In the infinitely dilute solution limit, the reference experimental values for the longest relaxation time τ_1 and equilibrium chain size R_c are $\tau_1 = 7.2 \times 10^{-4}$ s and $R_c = 3.008 \times 10^{-5}$ cm.[21,40] In our calculations, the PEO chain is discretized into $N_b = 41$ beads with original chain length at 0.7 of maximum. We have employed the same numerical methods as in Ref. 35. All shown theoretical results involve averages over 100 evolutions.

The first two sets of runs involve identical hydrodynamic interactions and intermolecular forces but different elasticity laws. Since our aim is to test the merits of the Pincus-FENE elasticity law in comparison with the FENE law, they do not include entanglements. The corresponding chain length ver-
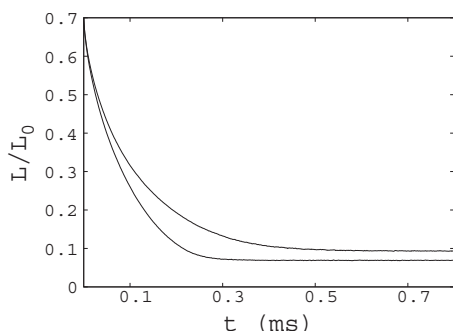
FIG. 4. Normalized chain length vs time for FENE (low curve) and Pincus-FENE (upper curve) elasticity laws. The Pincus-FENE law provides larger equilibrium chain sizes and longer relaxation times offering, overall, better agreement with experiment.

TABLE I. Comparison of theoretical and experimental longest relaxation times τ_1 and equilibrium chain sizes R_c. The full combination of the Pincus–FENE elasticity, coarse-grained IMFs and ECD agrees very well with experiment. The results are obtained without any parameter tuning and point out that the correct capturing of excluded volume effects requires the combined IMF and ECD action.

41 beads	τ_1 ($\times 10^{-4}$ s)	R_c ($\times 10^{-5}$ cm)
FENE (IMF, no ECD)	0.491	1.276
Pincus-FENE (no IMF, no ECD)	1.040	1.046
Pincus-FENE (IMF, no ECD)	0.984	1.557
Pincus-FENE (no IMF, ECD)	0.981	0.482
Pincus-FENE (IMF, ECD)	7.391	3.052
Experiment	7.2	3.008

sus time curves is shown in Fig. 4. Applying standard methods, we find (Table I) $\tau_1=0.491\times10^{-4}$ s and $R_c=1.276\times10^{-5}$ cm for the FENE case, and $\tau_1=0.984\times10^{-4}$ s and $R_c=1.557\times10^{-5}$ cm for the Pincus-FENE case. Evidently, the Pincus-FENE law results compare somewhat better with experiment. This is because, for $r<r^\star$, the Pincus law predicts smaller elastic forces[36] than the corresponding ideal chain elasticity law. Thus, the balance of excluded volume (IMF) and elastic forces changes in favor of the former slowing down the (elasticity driven) rate of chain length retraction (hence increasing τ_1), and augmenting chain swelling at equilibrium (hence increasing R_c). Indeed, this was the motive for introducing the Pincus-FENE law in our stochastic dynamics model in the first place.

Having established the usefulness of the Pincus-FENE model, we now investigate the merits of our combined (IMF plus ECD) treatment of excluded volume effects. Thus, we repeat the above mentioned Pincus-FENE run with the inclusion of intrachain self-entanglement effects. As shown in Fig. 5 (left), this has a dramatic effect on the results. The entanglements are responsible for a new, significantly slower relaxation mode that results in $\tau_1=7.391\times10^{-4}$ s. Moreover, entanglement induced excluded volume effects enhance chain swelling and lead to a larger equilibrium chain size $R_c=3.052\times10^{-5}$ cm. The new slower relaxation mode is explained as follows: for the majority of the chain relaxation curve, the entanglements are not important since (due to the

stretched state of the chain) the various parts of the polymer remain far apart. However, during the last stages of relaxation, the chain shrinks enough for Brownian motion effects to cause entanglements between different chain segments. Indeed, Fig. 5 (left) shows explicit association between the new relaxation mode, curve (b), and the rise and equilibration of the number of entanglements Π, curve (a). On the other hand, noticing that ECD encodes hard, contact potentials that make a positive contribution to the excluded volume, the observed R_c growth appears fully plausible. Notably, the sharp polymer length rebound before the final relaxation period is a consequence of the initial condition of a straight extended chain. Initial conditions with disordered stretched chains would result in smoother evolutions but allow the same conclusions since the final relaxation period (of interest here) is not affected. Remarkably, the results match the experimental values without any parameter tuning. Moreover, in agreement with arguments set forth in reference,[35] *both* entanglements and intermolecular force contributions to excluded volume effects are necessary for this good agreement. In order to demonstrate better the last point, we show in Fig. 5 (right) four length versus time curves with the Pincus-FENE model: (a) with both ECD and IMF, (b) with IMF but no ECD, (c) with ECD but no IMF, and (d) without any excluded volume effects (i.e., without ECD and IMF). Evidently, the very good agreement between theory and ex-
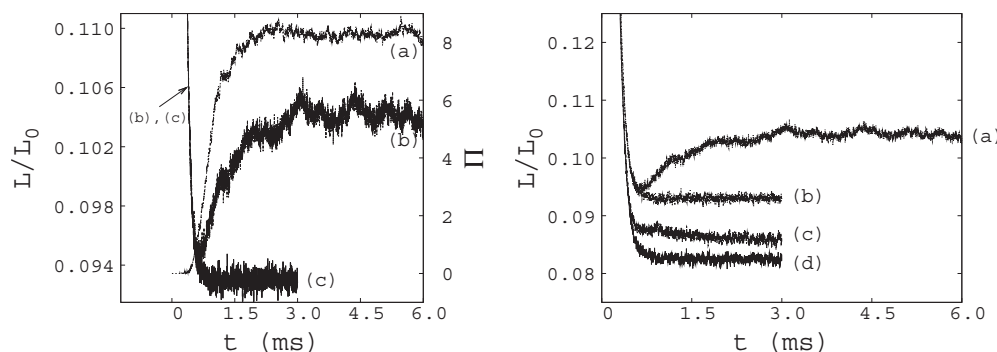

FIG. 5. Results of polymer relaxation computations with stochastic dynamics including Pincus-FENE elasticity and hydrodynamic interactions. Left: polymer length vs time curves: (c) IMF but no ECD and (b) IMF and ECD. Curve (a) shows the number of entanglements Π vs time for the ECD case. Evidently, entanglements are associated with a new (in comparison with phantom chain dynamics), slower relaxation mode that leads to very good agreement between theory and experiment. Right: polymer length vs time curves: (a) with both IMF and ECD, (b) with IMF but without ECD, (c) without IMF but with ECD, and (d) without IMF or ECD. It is the combined IMF and ECD action that results in very good agreement between theory and experiment.

TABLE II. Tests of robustness of model predictions under variation of the number of beads per chain. IMF signifies intermolecular forces and ECD is entangled chain dynamics. Although predictions with entangled chain dynamics (right) appear more sensitive to variation of the number of beads, they allow similar conclusions.

Pincus-FENE	τ_1 ($\times 10^{-4}$ s)	R_c ($\times 10^{-5}$ cm)
(IMF, no ECD)		
31 beads	1.01	1.58
41 beads	0.98	1.55
51 beads	0.87	1.51
(IMF, ECD)		
31 beads	8.8	2.0
41 beads	7.3	3.0
51 beads	7.0	4.1
Experiments	7.2	3.0

periment for both τ_1 and R_c requires both mechanisms. It is important to note that as expected, the number of entanglements at equilibrium increases (by a factor of 3) in the absence of any IMF forces, since, in this case, chains approach each other unhindered. However, this (purely ECD) version of the model does not appear physically plausible since, in comparison with case (d), it leads to larger chain lengths but smaller end-to-end distances (see chain sizes in Table I). This behavior is associated with unphysically tangled chain conformations that do not posses the correct amount of swelling.

We have also performed calculations checking the robustness of our results upon variation of the number of beads per chain. We have performed two sets of runs with N_b =[31,41,51]. Only the second set includes entanglement effects. All computations employ the Pincus-FENE constitutive law and include intermolecular forces. Table II (top) indicates small variations of the results with the chosen resolution in phantom chain dynamics. Although the addition of entanglements (Table II, bottom) is accompanied by a larger variation of the results, our major conclusions are not affected. The notable trend toward smaller longest relaxation times with increasing N_b is explained by observing the number of entanglements versus time in all three cases (Fig. 6, left). The larger the number of springs, the greater the
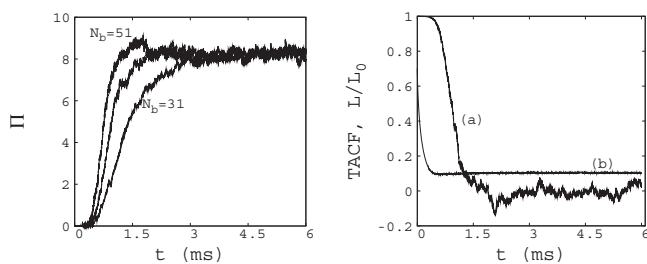
chances of contacts during relaxation, thus, understanding intuitively each entanglement as a chain collision, the faster the equilibration of the system.

Finally, it is important to note that our method of finding the longest relaxation time is based on the chain length relaxation curve (CLRC) and an exponential fit of its final period that corresponds to 10% of the maximum length. There is an alternative method of quantifying the longest relaxation time. It is based on the computation of the time autocorrelation function (TACF) of the unit vectors pointing along the chain end-to-end direction. This function is fitted with a stretched exponential function, and the area under the curve is interpreted as the mean chain orientation relaxation time (providing an approximation to the longest relaxation time).[41] In Fig. 6 (right), we plot the CLRC and TACF functions versus time for the N_b=41, Pincus-FENE (IMF and ECD) case (Table I). Evidently, for our initial conditions, chain length reaches an equilibrium value long before chain orientation does. Notably, the TACF based τ_1 values are greater (typically by an order of magnitude) than the CLRC based ones for the various cases of Table I. The only remarkable exception is the full physics case, i.e., Pincus-FENE (IMF and ECD), where the TACF value $\tau_1 \approx 9.16 \times 10^{-4}$ s is similar to the CLRC value $\tau_1 \approx 7.39 \times 10^{-4}$ s. Since the equilibration of length signifies the end of chain stretch and the associated elastic stress build-up, we think that the CLRC values are more suitable for the analysis of extensional rheology problems.

IV. SOLUTION METHODS FOR PERIODIC FLOW DOMAINS

Now that the merits of the model have been demonstrated, we show how to solve it in periodic flow domains. In this way, finite polymer mass concentration effects can be studied. The methods can be divided into the numerics and informatics categories. The latter (including data structures and algorithms) are far from trivial and although their detailed exposition is not possible within the limits of the present paper, we discuss the main issues and their algorithmic resolution.

On the numerics side, we note that the exponential decay of the intermolecular forces on the (equilibrium) spring size scale allows the application of the minimum image method in their computation without loss of accuracy.[42] Thus, there are only two main numerical problems: (a) the solution of the delta function forced Stokes equation and (b) the computation of ECD in periodic domains. Regarding the first, we have applied the method of Hernández-Ortiz et al. which was excellently discussed in Ref. 43. Their approach incorporates Fixman's idea of employing Chebyshev interpolation in the computation of Brownian motion effects,[13,20] thus, it does not involve an explicit construction of the diffusion matrix. On the other hand, the method requires the solution of the Stokes equations [with the smooth part of $\boldsymbol{\rho}(\mathbf{x})$ decomposition] in periodic domains. We have employed a standard approach reducing the solution of the latter equation to the solution of four Poisson equations in periodic domains (one for pressure and one for each of the three velocity compo-

FIG. 6. Left: number of entanglements Π vs time t for three different resolutions N_b=[31,41,51] of entangled chain dynamics. Although the final number of entanglements is similar in all cases, better resolved cases correspond to larger values of Π at intermediate times. Right: normalized chain length relaxation curve (b) and time autocorrelation function (a) for entangled chain dynamics with N_b=41. Chain orientation relaxes to equilibrium more slowly than chain length.
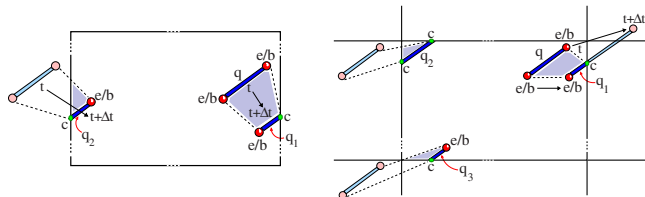
FIG. 7. The crossing of boundaries by a connector q results in the introduction of cutpoints. Here, e/b denotes an entanglement or bead, c is a cutpoint, and the arrows from t to $t+\Delta t$ indicate connector motion within time Δt. In the crossing of a corner case (right) the wrapping of connector q at time $t+\Delta t$ back inside the computational domain (as dictated by the periodic boundary conditions) results in the appearance of three disconnected segments q_1, q_2, and q_3. For the purpose of assigning entanglement volumes to them, the latter are considered evolutions of virtual connectors (indicated with faint lines).

FIG. 8. Chain conformations of polymers in a dense solution with polymer mass concentration $c=1.33\times10^{-2}$ g/cm^3. The polymer volume fraction ϕ is $\phi\approx6.1594\phi_e$, where ϕ_e is the entanglement concentration volume fraction. The system size is $l_b=0.998\times10^{-5}$ cm. At this time instant, there are 648 beads, 135 entanglements, and 116 cutpoints. For clarity, bead positions are left unmarked. The filled circles indicate cutpoint positions and the empty circles are entanglement positions. A triple wrapping case is pointed out by circling the four connectors that correspond to the fragments of a boundary-crossing connector (denoted by q in Fig. 7). Fragment q_1 is the initial part of connector q and fragment q_4 is its final part.

nents). Our Poisson solver reduces the analytical problem to an algebraic one by central differencing the second derivatives on a N_p^3 grid. Subsequently, it solves the obtained algebraic equations via fast Fourier transforms.[44]

Regarding ECD, care is needed when a connector q (Fig. 7, left) approaches the boundary of the flow domain. In computations with point particles, a particle crossing a periodic boundary reappears from the "opposite" side. In the polymer case, a boundary-crossing connector creates a "cutpoint" c (an end point of connector q_1 in Fig. 7, left) and a second connector q_2 on the opposite boundary (involving c's twin cutpoint). Thus, we have two chain segments (when previously we had one) and we need to assign the correct entanglement volumes V^{ij} to each one of them in order to avoid the agglomeration of spurious entanglements close to the boundaries. Our method considers the first cutpoint connector q_1 as the evolution of the initial crossing connector q, and the second cutpoint connector q_2 as the evolution of the virtual periodic image of q (shown with faint lines and outside the main domain in Fig. 7). The shaded regions indicate the areas within the computational domain scanned by the connectors, i.e., regions where new entanglements could be detected. Things become complicated near corners (Fig. 7, right): It is possible for a connector q to generate two (and in the general three-dimensional case, up to three) new pairs of cutpoints. In this case, the new connectors are considered evolutions of virtual copies of q whose positions are defined by following the required directional "jumps" that wrap the crossing connector q back inside the computational domain. In Fig. 8, we present results from an actual computation pointing out entanglement and cutpoint positions, as well as indicating a triple connector wrapping case. Such events are very common, and, if not treated properly, lead to spurious entanglements that invalidate the calculation. The reverse processes appear when a "broken" connector becomes whole again after completely crossing a boundary. The corresponding V^{ij} assignments follow directly from the above discussion.

On the informatics side, we note that the algorithmic complexity of the above discussed ECD numerics is significant. There are three different kinds of objects in the theory: beads, entanglements, and cutpoints. One needs data structures for storing their position and order of occurrence along
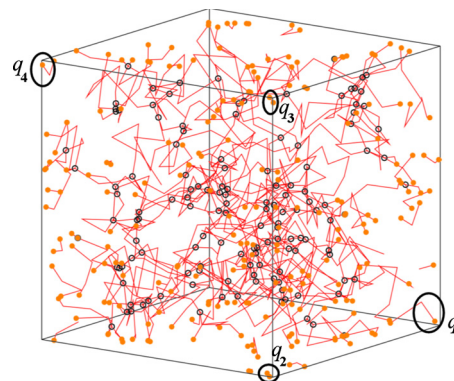
the chains. We have found that upon entanglement creation, it is efficient to add two entanglement labels to the data structure tracking order (one for each chain involved) while adding, of course, only one position. This allows better tracking of the objects composing a chain, and easier implementation of the algorithms that remove entanglements from the data structures (including resorting of all the remaining objects). When it comes to cutpoints, the opposite strategy is followed: each new cutpoint addition requires the insertion of only one new label in the order tracking data structure but two positions (one for each opposite side of the computational domain as Fig. 7 shows). Since in this way, two distinct cutpoints have the same label, we bestow each chain with a definite direction and distinguish the twin cutpoints by their order of appearance as one moves from chain start to chain end.

The overall information flow chart includes the following steps: starting from the initial conditions, (1) update the bead positions via Langevin dynamics, (2) update entanglement positions by optimizing the elastic energy of the system, (3) apply periodic boundary conditions to beads and entanglements by employing the standard approach of point molecular dynamics, (4) search for new cutpoints or remove old ones while changing, as needed, the entanglement volumes of all segments, (5) create/annihilate entanglements, (6) remesh entanglements where necessary by passing them over neighboring objects, and (7) repeat the above until the end computational time. A key point here is that both steps (5) and (6) require parallel cutpoint remeshing and entanglement volume readjustment in addition to similar operations performed during step (4) above.

V. FINITE CONCENTRATION SOLUTIONS

Having indicated the plausibility of our model and shown how to solve it in periodic flow domains, we apply it here to the computation of entangled polymer solutions in equilibrium. Our working solution is the aqueous PEO solu-
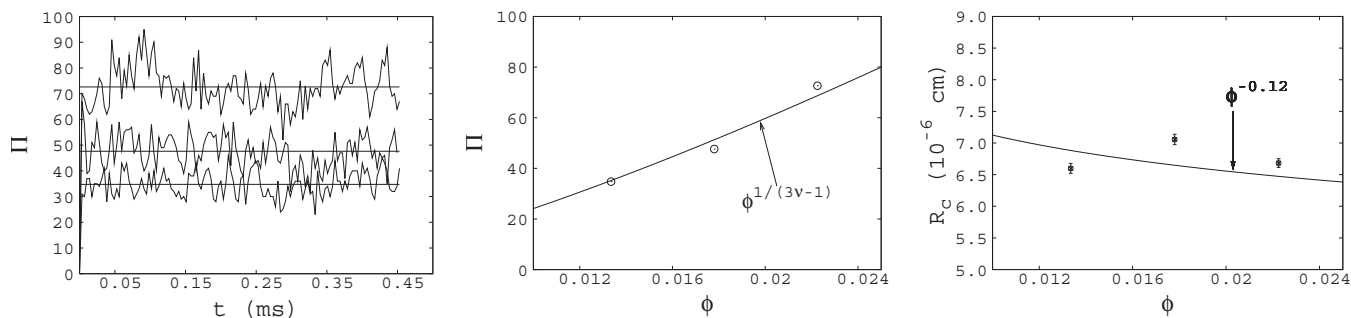
FIG. 9. Left: number of entanglements Π vs time t. In all cases, after a short transient, the system reaches an equilibrium. The solid lines indicate the time averaged values. Center: number of entanglements Π vs polymer volume fraction ϕ. The results reproduce very well the tube-theoretic scaling $\phi^{1/(3\nu-1)}$. Right: chain end-to-end distance R_c vs polymer volume fraction ϕ (including the error bars of the numerical fit). All R_c values are much smaller than the corresponding $R_c = 3.0 \times 10^{-5}$ cm value in the infinitely dilute solution limit. In this way, the results support Flory's intuition about the screening of excluded volume effects in dense solutions. The solid line indicates the expected $\phi^{-0.12}$ scaling of R_c assuming the latter.

tion studied above. Since it is important to study the variation of quantities of interest with concentration, we consider three different polymer volume fractions ϕ. Unfortunately, computational complexity does not allow us to specify a wide ϕ range within reasonable run-times. We present results with three different volume fractions, all above the entanglement concentration threshold $\phi_e = 5.78 \times 10^{-3}$. In particular, since our computational domain has size $l_b = 0.998 \times 10^{-5}$ cm, we employ $N_c = 3$ for $\phi = 2.30\phi_e$, $N_c = 4$ for $\phi = 3.07\phi_e$, and $N_c = 5$ for $\phi = 3.84\phi_e$. For comparison, the overlap concentration volume fraction is $\phi^\star = 0.23\phi_e$ and the concentrated solution volume fraction is $\phi^{\star\star} = 64.96\phi_e$.

As remarked already, we need to take advantage of our finer (compared to tube theory) mesoscopic viewpoint in order to resolve some basic space-time scales. Fundamental length scales are the tube sizes a which, for the three different concentrations, are $a_3 = 7.0 \times 10^{-6}$ cm, $a_4 = 5.6 \times 10^{-6}$ cm, and $a_5 = 4.7 \times 10^{-6}$ cm, where the subscripts correspond to the number of chains. In computing a, we employ the formula $a(\phi) = a(1)\phi^{\nu/(3\nu-1)}$ (Ref. 2) (athermal solvent) which predicts tube sizes that are proportional, although larger, than the correlation length ξ. For an athermal solvent, ξ describes the distance between intermolecular contacts. The tube size in a melt is $a(1) \approx b_K\sqrt{N_e(1)}$, where $N_e(1)$ is the number of Kuhn monomers in an entanglement strand in a melt [$N_e(1) = 13$ for our polymer]. We employ the finest, yet still computationally feasible, resolution of the a scale. Thus, starting from the most demanding case of $\phi = 3.8496\phi_e$, we find that the choice $N_b = 81$ gives equilibrium spring size $R_s = 1.1 \times 10^{-6}$ cm, which corresponds to ratio $a/R_s = 4.262$, i.e., the tube size is well resolved. Moreover, for the same ϕ, the number of monomers in an entanglement strand is $N_e(\phi) = 1893$, which is much larger than the number of monomers in a spring $N_s = 138$. The reference time scale is the entanglement strand relaxation time $\tau_e = 1.0 \times 10^{-4}$ s. Since our time step is $\delta t = 10^{-2}\tau_s$ (where $\tau_s = 3.5 \times 10^{-7}$ s is the equilibrium spring relaxation time) τ_e is also well resolved. Notably, since R_s is smaller than the solution correlation length, τ_s incorporates both Zimm and Flory theories. Finally, the Poisson solver computational grid size is $N_p = 16$.

Figure 9 (left) shows the predicted number of entanglements Π versus time t for the three concentrations of interest.

Evidently, our method treats boundary effects appropriately since in all cases, the system reaches an equilibrium. This is a first, nontrivial achievement of the underlying complex algorithmic structure. The computations ended when the time series for polymer length and entanglements reached an evident equilibrium for all concentrations. The averages were formed by averaging the equilibrium time series in time.

Let us first note that as discussed in Ref. 35, our "primitive" entanglements are not identical with the "effective" entanglements of tube theory. This is because not all of the primitive entanglements are dynamically important in extensional flows. Indeed, as shown in the polymer knot stretching computations of Ref. 35, some of them correspond to trivial chain contacts. Therefore, we expect Π to be larger but of the same order of magnitude as its tube-theoretic analog. It is also important to note that tube-theoretic estimates of Π refer to the plateau region of step-strain experiments (i.e., to out-of-equilibrium solutions relaxing on the scale of the reptation time) while our present results refer to equilibrium. Nevertheless, in order to analyze better the potential of our new approach, it is instructive to compare our Π with tube-theoretic estimates. A key point of interest is to examine how the present scaling of Π with ϕ compares with the tube-theoretic one. In order to compute the latter, we first compute the number of Kuhn monomers in an entanglement strand $N_e(\phi) = N_e(1)\phi^{-1/(3\nu-1)}$ (Ref. 2) (athermal solvent), then find the number of entanglements per chain $N_{K,c}/N_e$, and finally, multiply with the number of chains in our computational domain. Accordingly, $\Pi_3 = 9$, $\Pi_4 = 18$, and $\Pi_5 = 30$. By averaging the results shown in Fig. 9 (left), we find that our model predicts $\langle \Pi_3 \rangle = 35$, $\langle \Pi_4 \rangle = 48$, and $\langle \Pi_5 \rangle = 73$. These values compare well (up to a plausible scaling factor of order one) with the corresponding tube theory values. Equally important, the data also exhibit the empirical scaling behavior of Π with ϕ (Fig. 9, middle).

Another important physics issue has to do with Flory's suggestion of excluded volume interaction screening on scales above the correlation length ξ. In this way, the size of a chain is approximated by a random walk of correlation blobs. Since increasing ϕ reduces ξ, one expects that more and more (with increasing ϕ) the chain size would tend to obey the theta solvent scaling. Indeed, the chain size diminishes until $\phi^{\star\star}$ is reached and its further reduction is impos-

sible since at $\phi^{\star\star}$, the correlation blobs become thermal blobs and the whole chain obeys the theta solvent scaling with no swelling whatsoever. Following the standard Flory theory, the variation of the chain size with ϕ is $R_c \approx b_K(v_{ev}/b_K^3\phi)^{(\nu-1/2)/(3\nu-1)}N_{K,c}^{1/2}$.[2] Employing $\nu=0.588$, we find $R_c \sim \phi^{-0.12}$. For the three studied volume fractions, we have R_c of $(1.13\times10^{-5}, 1.10\times10^{-5}, 1.07\times10^{-5})$ cm for $N_c=(3,4,5)$, while our model predicts $(0.65\times10^{-5}, 0.70\times10^{-5}, 0.66\times10^{-5})$ cm, respectively. These values agree up to a plausible factor 0.5 with the corresponding Flory theory values. All computed R_c are much smaller than the chain size in the infinitely dilute solution limit, $R_c=3.05\times10^{-5}$ cm. Equally important, the data approximate reasonably well the scaling behavior of R_c with ϕ (Fig. 9, right) that is expected on the basis of excluded volume force screening. In this way, the predictions of our theory vindicate Flory's intuition.

VI. CONCLUSION

We have proposed an entangled chain dynamics model of dense polymer solutions. The model includes the self-consistent dynamics of polymer chains and solvent by describing the former via coarse-grained molecular dynamics that incorporate hydrodynamic interaction effects, and the latter via the forced Stokes equation. Excluded volume effects are modeled via the combined action of coarse-grained intermolecular potentials and explicit geometric tracking of chain entanglements. The governing equations do not include any adjustable constants and require only standard material properties as input. We have found that entanglements are responsible for a new (compared to phantom chain computations) slow relaxation mode whose characteristic time scale agrees very well with experiment. Similarly good agreement between theory and experiment was also obtained for the chain size. Since the full potential of the new model can only be realized in finite polymer mass concentration solutions, we have developed methods for its solution in periodic flow domains. In this milieu, the most challenging difficulty has to do with the correct computation of ECD, i.e., with finding a method that avoids spurious entanglements next to the flow domain boundaries. Our method introduces a new kind of object, the cutpoints that keep track of the intersections of polymer chains with the periodic boundaries. By keeping track of all changes that the insertion and deletion of cutpoints induce in the entanglement volume function that decides the introduction or removal of entanglements, we are able to compute the equilibrium state of dense polymer solutions of various concentrations. We have shown that the computed number of entanglements Π agrees well with the number of entanglements expected on the basis of tube theory, satisfactorily reproducing the latter's scaling of Π with the polymer volume fraction ϕ. Furthermore, our model predicts diminishing chain size with concentration, thus vindicating Flory's suggestion of excluded volume effects screening in dense solutions. The predicted scaling of chain size with ϕ is consistent with the heuristic, Flory theory based value.

In the future, the present model and methods could be applied to the investigation of fundamental problems in dense solution rheology, for example, step-strain relaxation experiments or extensional viscoelastic flows. Taking into account that the model's predictions agree well with experiment without the need of adjustable constants, it appears that its connection with more microscopic physics is well founded. On the other hand, the present results encourage further work on the systematic grounding of tube-theoretic ideas on more microscopic stochastic dynamics models similar to ours. Eventually, one aims to demonstrate that the approach set out in this work could reliably predict the dynamics of polymeric fluids at high strain rates without any prior input from special purpose experiments. This would require the introduction of stable implicit integration schemes that would preserve the maximum chain length limit during strong polymer extensions.

Our good results regarding longest relaxation time and equilibrium chain size invite investigation as to whether this kind of predictive power is general for any linear chain of any molecular weight. In this context, we note that another problem of great importance is the prediction (depending on temperature and concentration) of phase transitions (mesophases) in polymer solutions. While such matters are faithfully investigated via microscopic, atomistic dynamics, the employment of effective, coarse-grained (CG) intermolecular force potentials allows the calculation of system evolution for larger times. This is because in comparison with fundamental interactions, CG potentials decay faster (thus a smaller set of neighbors of each particle need to be considered when computing the forces on the latter) and are smoother (allowing larger numerical times steps).[45] Our CG potential satisfies these requirements, and, by requiring only standard material properties as input, could be employed in order to parametrize intermolecular forces at arbitrary polymer CG scales. In this way, it could be a suitable alternative to CG Lennard-Jones potentials employed in various phase transition investigations.[45,46]

Finally, we note that a natural continuation of the present work would be to employ a Green–Kubo type of relations and by computing the autocorrelation of the symmetrized traceless part of the equilibrium stress tensor to obtain the relaxation modulus. Taking into account the computational complexity of the present calculations, such developments would require the parallelization of our algorithms which, due to data dependencies introduced by the entanglements, is a nontrivial task.

[1] R. B. Bird, C. F. Curtiss, R. C. Armstrong, and O. Hassanger, *Dynamics of Polymeric Liquids* (Wiley-Interscience, New York, 1989).
[2] M. Rubinstein and R. H. Colby, *Polymer Physics* (Oxford University Press, Oxford, 2003).
[3] T. Kawakatsu, *Statistical Physics of Polymers* (Springer, Berlin, 2004).
[4] R. G. Larson, *The Structure and Rheology of Complex Fluids* (Oxford

University Press, Oxford, 1999).

[5] P. Oswald, *Rheophysics: The Deformation and Flow of Matter* (Cambridge University Press, Cambridge, 2009).

[6] M. Griebel, S. Knapek, and G. Zumbusch, *Numerical Simulation in Molecular Dynamics: Numerics, Algorithms, Parallelization, Applications* (Springer, Berlin, 2007).

[7] N. C. Karayiannis and M. Kröger, Int. J. Mol. Sci. **10**, 5054 (2009).

[8] H. C. Öttinger, *Stochastic Processes in Polymeric Fluids* (Springer, Berlin, 1996).

[9] I. Snook, *The Langevin and Generalized Langevin Approach to the Dynamics of Atomic, Polymeric and Colloidal Systems* (Elsevier Science, Amsterdam, 2007).

[10] R. M. Mazo, *Brownian Motion: Fluctuations, Dynamics, and Applications* (Oxford University Press, Oxford, 2002).

[11] W. T. Coffey, Yu. P. Kalmykov, and J. T. Waldron, *The Langevin Equation: With Applications to Stochastic Problems in Physics, Chemistry and Electrical Engineering* (World Scientific, Singapore, 2004).

[12] D. L. Ermak and J. A. McCammon, J. Chem. Phys. **69**, 1352 (1978).

[13] M. Fixman, Macromolecules **19**, 1204 (1986).

[14] P. S. Grassia, E. J. Hinch, and L. C. Nitsche, J. Fluid Mech. **282**, 373 (1995).

[15] P. S. Grassia and E. J. Hinch, J. Fluid Mech. **308**, 255 (1996).

[16] C. Hsieh, L. Li, and R.G. Larson, J. Non-Newtonian Fluid Mech. **113**, 147 (2003).

[17] J. S. Hur, E. S. G. Shaqfeh, and R. G. Larson, J. Rheol. **44**, 713 (2000).

[18] R. M. Jedrejack, M. D. Graham, and J. J. de Pablo, J. Chem. Phys. **113**, 2894 (2000).

[19] M. Kröger, A. Alba, M. Laso, and H. C. Öttinger, J. Chem. Phys. **113**, 4767 (2000).

[20] A. J. Banchio and J. F. Brady, J. Chem. Phys. **118**, 10323 (2003).

[21] D. Kivotides, V. V. Mitkin, and T. G. Theofanous, J. Non-Newtonian Fluid Mech. **161**, 69 (2009).

[22] S. F. Edwards, Proc. Phys. Soc. London **91**, 513 (1967).

[23] M. Doi and S. F. Edwards, *The Theory of Polymer Dynamics* (Oxford University Press, Oxford, 1986).

[24] P. G. de Gennes, Macromolecules **17**, 703 (1984).

[25] P. G. de Gennes, J. Chem. Phys. **55**, 572 (1971).

[26] G. Marrucci, Science **301**, 1681 (2003).

[27] A. E. Likhtman and R. S. Graham, J. Non-Newtonian Fluid Mech. **114**, 1 (2003).

[28] S. T. Milner, T. C. B. McLeish, and A. E. Likhtman, J. Rheol. **45**, 539 (2001).

[29] R. S. Graham, A. E. Likhtman, T. C. B. McLeish, and S. T. Milner, J. Rheol. **47**, 1171 (2003).

[30] K. K. Kabanemi and J.-F. Hétu, J. Non-Newtonian Fluid Mech. **160**, 113 (2009).

[31] J. N. Israelachvili, *Intermolecular and Surface Forces* (Academic, Amsterdam, 1992).

[32] S. Kumar and R. G. Larson, J. Chem. Phys. **114**, 6937 (2001).

[33] S. P. Holleran and R. G. Larson, Rheol. Acta **47**, 3 (2008).

[34] J. T. Padding and W. J. Briels, J. Chem. Phys. **115**, 2846 (2001).

[35] D. Kivotides, S. L. Wilkin, and T. G. Theofanous, Phys. Rev. E **80**, 041808 (2009).

[36] P. Pincus, Macromolecules **9**, 386 (1976).

[37] S. Kim and S. J. Karrila, *Microhydrodynamics* (Dover, Mineola, 2005).

[38] C. Pozrikidis, *Boundary Integral and Singularity Methods for Linearized Viscous Flow* (Cambridge University Press, Cambridge, 1992).

[39] N. M. Toan and D. Thirumalai, Macromolecules **43**, 4394 (2010).

[40] V. Tirtaatmadja, G. H. McKinley, and J. J. Cooper-White, Phys. Fluids **18**, 043101 (2006).

[41] G. D. Smith and D. Bedrov, J. Non-Cryst. Solids **352**, 4690 (2006).

[42] S. Pfalzner and P. Gibbon, *Many-Body Tree Methods in Physics* (Cambridge University Press, Cambridge, 2005).

[43] J. P. Hernández-Ortiz, J. J. de Pablo, and M. D. Graham, Phys. Rev. Lett. **98**, 140602 (2007).

[44] W. H. Press, B. P. Flannery, S. A. Teukolsky, and W. T. Vetterling, *Numerical Recipes* (Cambridge University Press, Cambridge, 1992).

[45] S. J. Marrink, A. H. de Vries, and A. E. Mark, J. Phys. Chem. B **108**, 750 (2004).

[46] E. R. May, D. I. Kopelevich, and A. Narang, Biophys. J. **94**, 878 (2008).